ACS APPLIED MATERIALS & INTERFACES

Research Article

www.acsami.org

Synthesis of Magnesium Oxide Hierarchical Microspheres: A Dual-Functional Material for Water Remediation

Swasmi Purwajanti, Liang Zhou, Yusilawati Ahmad Nor, Jun Zhang, Hongwei Zhang, Xiaodan Huang, and Chengzhong Yu*

Australian Institute for Bioengineering and Nanotechnology, The University of Queensland, Brisbane, Queensland 4072, Australia

Supporting Information

ABSTRACT: High concentration of heavy metals and microbes present in water can reduce the quality of water and bring serious side effects to human beings. Their removal from water is of great importance. In this study, MgO microspheres with hierarchical morphology have been synthesized by a facile and low-cost precipitation-aging-calcination method and their dual functionality for effective arsenic removal and microbial inhibition has been investigated for the first time. By systematical investigation on the synthesis, structure and performance relationship, optimized MgO microspheres are prepared with both high arsenic removal capacity and prominent antibacterial activity. Hierarchical MgO microspheres calcined at 500 °C exhibit the best trade-off between As(III) adsorption (502 mg g^{-1}) and antibacterial performance (complete elimination at 700 μg mL^{-1}). It is also demonstrated that our materials can be used for the simultaneous removal of arsenic and microbes in a model water system. This study offers a convenient and low cost dual-function agent with efficient performance for water treatment.

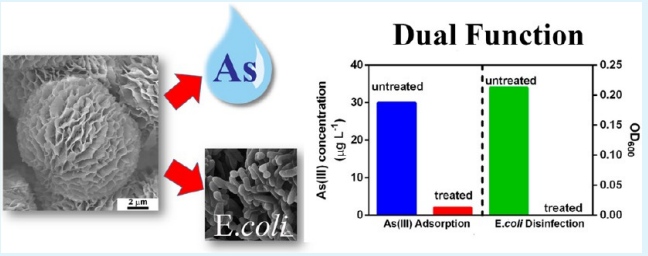

KEYWORDS: *hierarchical structure, magnesium oxide, adsorption, bacterial removal, dual function property*

INTRODUCTION

The lack of safe and clean water has become one of humanity's big problems.[1] Thousands of organic/inorganic compounds and microbes have been identified as water contaminants.[2] Heavy metals represent a typical class of contaminant in water resources. Some heavy metals are highly toxic and carcinogenic. Taking arsenic as an example, its contamination in groundwater and drinking water poses a big threat, affecting around 150 million people worldwide.[2] Microbes are another class of contaminant in water. Harmful microbes, such as bacteria, are the most notorious pathogens for humans and are responsible for causing waterborne diseases.[1,2] Considering these facts, the development of effective, low-cost and robust methods for decontamination and disinfection of water is one of the greatest global challenges.

Recently developed nanotechnology provides new opportunities in water remediation.[3] The desirable features of nanomaterials for water treatment include high surface area for adsorption.[3] Among the available nanomaterials, metal oxide nanostructures have attracted significant attention in water treatment.[4−11] Magnesium oxide (MgO) is an abundant, nontoxic, and environmentally friendly material, which has been used as an adsorbent to remove organic dyes,[12,13] phosphates,[14] and heavy metals.[12,15] Interestingly, MgO based adsorbents show exceptionally high arsenic adsorption capacity, superior to other metal oxides.[16−18] In addition, MgO has also been used as a disinfection agent, which shows strong antibacterial activity and produces no harmful disinfection byproduct.[19−21] However, previous studies focused individually on either adsorption or disinfection, there is no report on the dual-functionalities of MgO in both water decontamination and disinfection. Because the optimized structures for two performances may be different, such a study is important to the development of dual-functionalized MgO with compromised structures and functions for simultaneous water decontamination and disinfection applications.

In this study, we report a facile and low-cost synthesis of MgO hierarchical microspheres. The synthesis conditions of MgO hierarchical structures are optimized to allow for both high arsenic removal capacity and high antibacterial activity. To the best of our knowledge, this is the first report on dual-functionalized MgO for simultaneous water decontamination and disinfection.

EXPERIMENTAL SECTION

Materials. All chemicals were used as received without further purification. Magnesium chloride hexahydrates ($MgCl_2.6H_2O$), sodium carbonate (Na_2CO_3) were supplied from Chemsupply chemicals. $NaAsO_2$ was obtained from Sigma-Aldrich. The 400 ppm As (III) stock solution was prepared by dissolving a proper amount of $NaAsO_2$ in Milli-Q water.

Received: June 22, 2015
Accepted: September 8, 2015
Published: September 8, 2015

DOI: 10.1021/acsami.5b05553
ACS Appl. Mater. Interfaces 2015, 7, 21278−21286

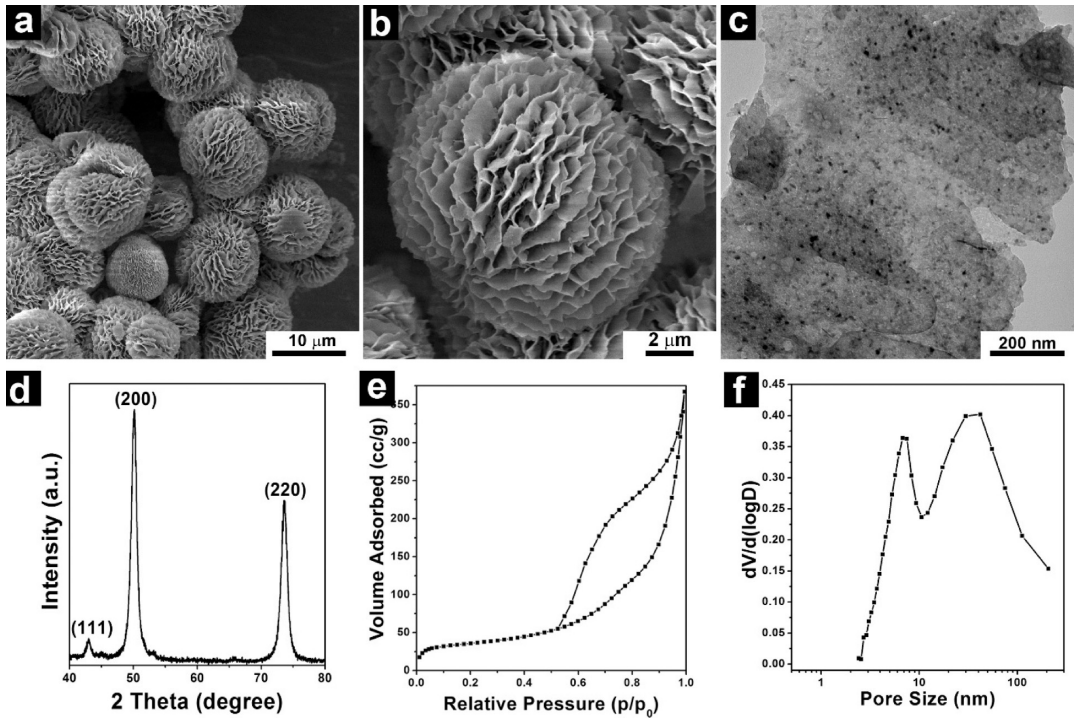

Figure 1. (a and b) SEM images, (c) TEM image, (d) XRD pattern, (e) N_2 adsorption isotherm, and (f) pore size distribution of MgO-500.

Synthesis. In a typical synthesis of MgO hierarchical microspheres: at room temperature, 25 mL of 1 M Na_2CO_3 solution was pumped into 25 mL of 1 M $MgCl_2{\cdot}6H_2O$ solution with a flow rate of 10.5 mL min^{-1} to form white precipitation. The white precipitate was aged in static condition at 80 °C for 2 h. The precipitate after aging was then washed with deionized water three times. The precipitate after aging and washing was donated as MgO-P. To obtain MgO, the as-prepared MgO-P was calcined in a muffle furnace at 500 °C for 5 h with temperature ramping rate of 2 °C min^{-1}. To study the effects of aging temperature and aging time on morphology of MgO-P, we varied the aging temperature from room temperature (RT) to 80 °C, while the aging time was varied from 0.5 to 120 min. To study the effects of calcination temperature on arsenic removal and antibacterial performance, we varied the calcination temperature from 400 to 700 °C, while other synthesis parameters were kept constant. The MgO samples prepared at a calcination temperature of 400, 500, 600, and 700 °C were denoted as MgO-400, MgO-500, MgO-600 and MgO-700, respectively.

Arsenic Adsorption. As(III) adsorption performance was studied by batch experiments with an adsorbent loading of 0.4 g L^{-1}. No pH adjustment was performed prior to the adsorption process. Typically, 20 mg of MgO was dispersed in 50 mL of As(III) solution with variable concentrations (50−400 mg L^{-1}), followed by shaking (200 rpm) at room temperature for 24 h to achieve equilibrium. After recovering the adsorbent by centrifugation and proper dilution into a particular concentration range, 5% of concentrated HNO_3 by volume was added into clear supernatant to preserve arsenic species. The As(III) was analyzed by inductively coupled plasma-optical emission spectrophotometry (ICP-OES) PerkinElmer Optima 7300DV with arsenic detection limits between 1 and 10 ppb.

The As(III) adsorption capacity was calculated using the following equation:

$$q_e = \frac{(C_0 - C_e)V}{m} \quad (1)$$

where C_0 and C_e represent the initial and the equilibrium As(III) concentration (mg L^{-1}), respectively. V is the volume of the As(III) solution (L) and m is the amount of adsorbent (g).

The effect of competing anions on arsenite adsorption capacity was studied in the presence of NaCl, Na_2CO_3, Na_2SiO_3 and Na_3PO_4 with a concentration of 1 g L^{-1}. The arsenic concentration was fixed at 400 mg L^{-1}, and the adsorbent dosage was 0.4 g L^{-1}.

Antibacterial Test. To study the antibacterial activity, the minimum inhibitory concentration (MIC) for the MgO samples was measured. *Escherichia coli* (DH5-α) was used as the microbial model existing in drinking water. *E. coli* was cultured in LB medium (Bacto-tryptone 10 g L^{-1}, Bacto-yeast extract 5 g L^{-1}, NaCl 10 g L^{-1}, pH = 7.2) at 37 °C on shaker bed at 200 rpm overnight. Then the concentration of bacteria, corresponding to an optical density (OD) of 0.1 at 600 nm for 1×10^8 CFU mL^{-1} was diluted with LB medium. Bacterial suspension (10% by volume), LB medium (80% by volume) and different concentration of particle diluted in PBS (10% by volume) were then mixed in centrifuge tube and shaken at 37 °C on shaker bed at 200 rpm for 24 h. Bacteria culture containing PBS only (in the absence of adsorbent) was included as a control experiment. After 24 h, the culture was centrifuged at 1000 rpm for 2 min and the supernatant was collected for OD measurement at 600 nm using multifunctional microplate reader (Tecan infinite M200).

Dual-Function Test. The dual functionality was tested using model contaminated water containing both As(III) (30 ppb) and *E. coli* (1×10^6 CFU mL^{-1}) which is above the maximum level contamination (MCL) set by the U.S. Environmental Protection Agency. MgO-500 (700 mg L^{-1}) was cultured in the model contaminated water for 24 h at 200 rpm at 37 °C. The supernatant was collected after centrifugation at 13000 rpm for 2 min and the As(III) concentration was measured by ICP-OES. Separately, the culture was centrifuged at 1000 rpm for 2 min and supernatant was collected for OD measurement at 600 nm using multifunctional microplate reader. The measurements were made in triplicates.

Characterization. The as-prepared MgO-P and MgO-400, MgO-500, MgO-600, and MgO-700 were comprehensively characterized using X-ray diffraction (XRD, Rigaku Miniflex X-ray Diffractometer with Ni-filtered Co Kα radiation (λ = 1.789 Å), operated at a voltage of 40 kV and a current 30 mA), scanning electron (Field emission-SEM JEOL 7800, operated at 5 kV) and transmission electron microscopy (TEM JEOL 1010, operated at 100 kV). The samples for TEM measurements were dispersed in ethanol by sonication and supported onto a holey carbon film on a copper grid. The N_2

DOI: 10.1021/acsami.5b05553
ACS Appl. Mater. Interfaces 2015, 7, 21278−21286

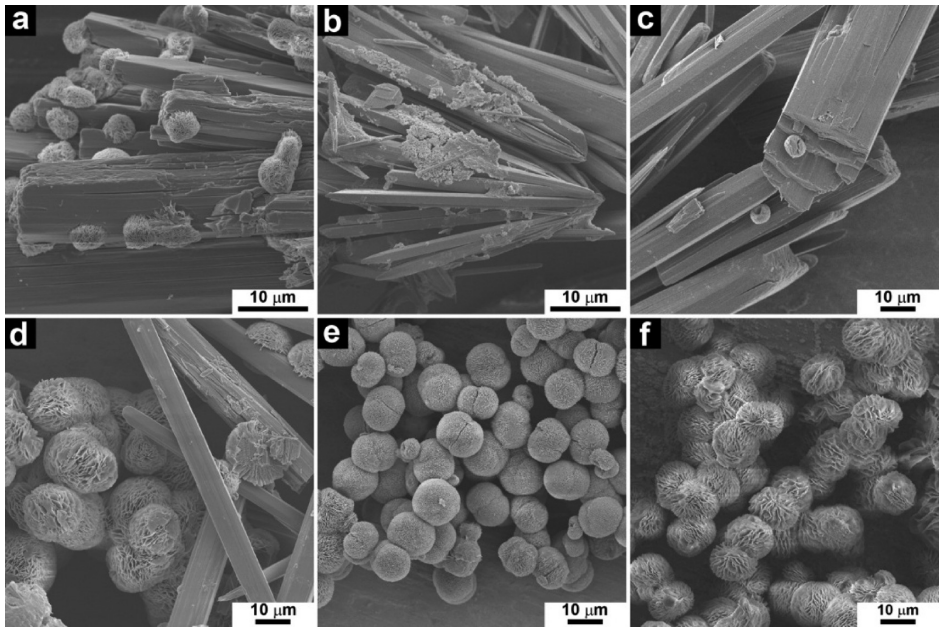

Figure 2. SEM images of MgO-P prepared at different aging temperatures: (a) RT, (b) 40, (c) 50, (d) 60, (e) 70, and (f) 80 °C.

adsorption−desorption isotherms were measured at 77 K using Micromeritics Tristar II 3020 surface area and porosity analyzer. The samples were degassed at 180 °C for 6 h before the measurement. The Brunauer−Emmet−Teller (BET) method was utilized to calculate the specific surface area. The pore distribution was derived from the adsorption branch of the isotherms using the Barret−Joyner−Halanda (BJH) method.

RESULTS AND DISCUSSION

Structure and Morphology of MgO. The MgO was synthesized by a facile and low-cost precipitation-aging-calcination method. Compared to the previous syntheses of hierarchical MgO nanostructures where the high temperature hydrothermal treatment is generally used,[16−18,22,23] lower synthesis temperatures and shorter aging time were employed in this study, representing a convenient and cost-effective synthesis strategy. After immediate mixing of Na_2CO_3 and $Mg(NO_3)_2{\cdot}6H_2O$, which is known as the precipitation process, nesquehonite ($MgCO_3{\cdot}3H_2O$, JCPDS Card No. 20-0669) was obtained (Figure S1). Aging the freshly prepared nesquehonite at 80 °C for 2 h converted it into hydromagnesite ($(Mg_5(CO_3)_4(OH)_2{\cdot}4H_2O$, JCPDS Card No. 25-0513) (Figure S2). Calcination in air such at 500 °C converted the hydromagnesite into MgO.

The synthesized MgO shows uniform microspherical morphology with a particle size of around 10 μm (Figure 1a). Each microsphere is constructed by a great number of nanosheets (Figure 1b). TEM observation on a typical nanosheet peeled off from the microspheres by sonication reveals that the nanosheet is composed of numerous nanograins (Figure 1c). Mesopores with small size (<10 nm) can be clearly observed. The nanocrystalline characteristic is further confirmed by XRD, where significant broadening of the diffraction peaks can be observed (Figure 1d). By applying the Scherer Equation to the most intensive (200) diffraction peak, the mean crystallite size of MgO is determined to be 10 nm, which can be attributed to the average thickness of nanosheets as building blocks to form the hierarchical microspheres.

The nanoporous nature of the sample was confirmed by N_2 adsorption analysis. The MgO hierarchical microspheres show a typical type-IV isotherm with H3 hysteresis loop, indicating a mesoporous nature (Figure 1e). Such a mesoporous structure leads to a surface area of 122 $m^2\ g^{-1}$, a pore volume of 0.57 $cm^3\ g^{-1}$, and two relatively broad pore size distribution centered at ~7.5 and 30−50 nm (Figure 1f). The origin of the smaller pores will be discussed in the section Effects of Calcination Temperature. The origin of larger pores with a broad distribution (10−100 nm) should be attributed to the voids formed by the packing of nanosheets or particles. Such a hierarchical micro/nanostructure is highly favorable in water treatment due to the synergistic effect of nanosized building blocks and micrometer-sized assemblies: while the nanosized building blocks provide high surface area and active sites for adsorption, the micrometer-sized assemblies provide desirable mechanical strength, facile mass transportation, and easy recovery.[6,16]

Effect of Aging Temperature. The aging temperature plays a significant role in governing the structure and morphology of the intermediates/products. To study the effects of aging temperature, we varied the aging temperature from RT to 80 °C while the aging time was kept at 120 min. Figure S3 shows the XRD patterns of MgO-P (the precipitate after aging and washing). A phase transformation from nesquehonite to hydromagnesite can be observed as the aging temperature increases from RT to 80 °C. From the XRD results, it can be concluded that the nesquehonite phase is thermodynamically unstable. It only exists at temperatures below 50 °C; at 60 °C, it begins to convert into hydromagnesite; the phase transformation from nesquehonite to hydromagnesite can be completed at 70 °C.

The phase transition is accompanied by an abrupt morphological change. Below 50 °C (Figures 2a−c), micrometer-sized rods are the dominant morphology. At a critical aging temperature of 60 °C, a mixture of microrods and hierarchical microspheres are obtained (Figure 2d). Above 70 °C, only hierarchical microspheres constructed by nanosheets can be observed (Figure 2e,f). Further calcination at a high

DOI: 10.1021/acsami.5b05553
ACS Appl. Mater. Interfaces 2015, 7, 21278−21286

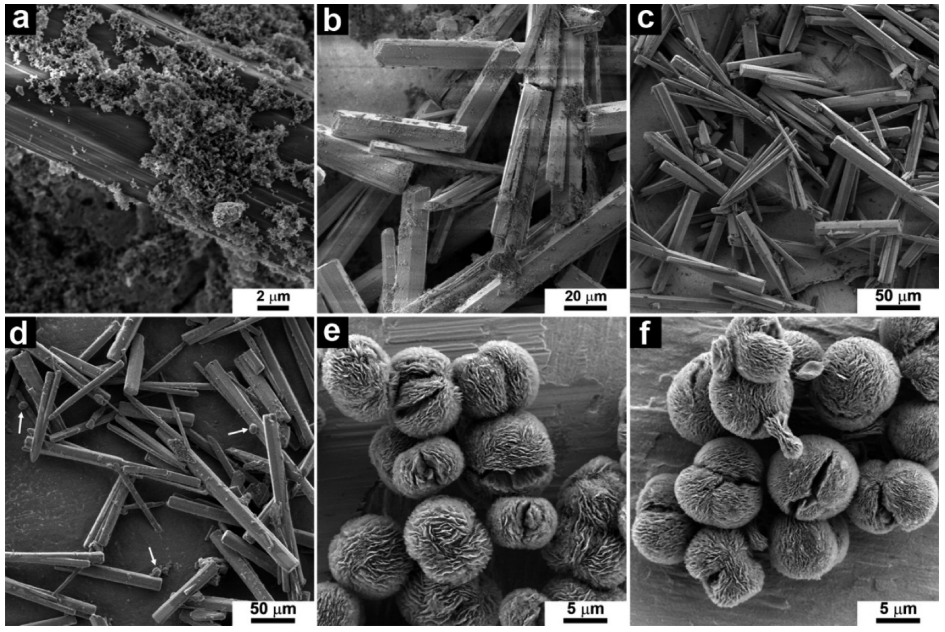

Figure 3. SEM images of MgO-P prepared at 80 °C with different aging time: (a) 0.5, (b) 2, (c) 5, (d) 10, (e) 20, and (f) 30 min.

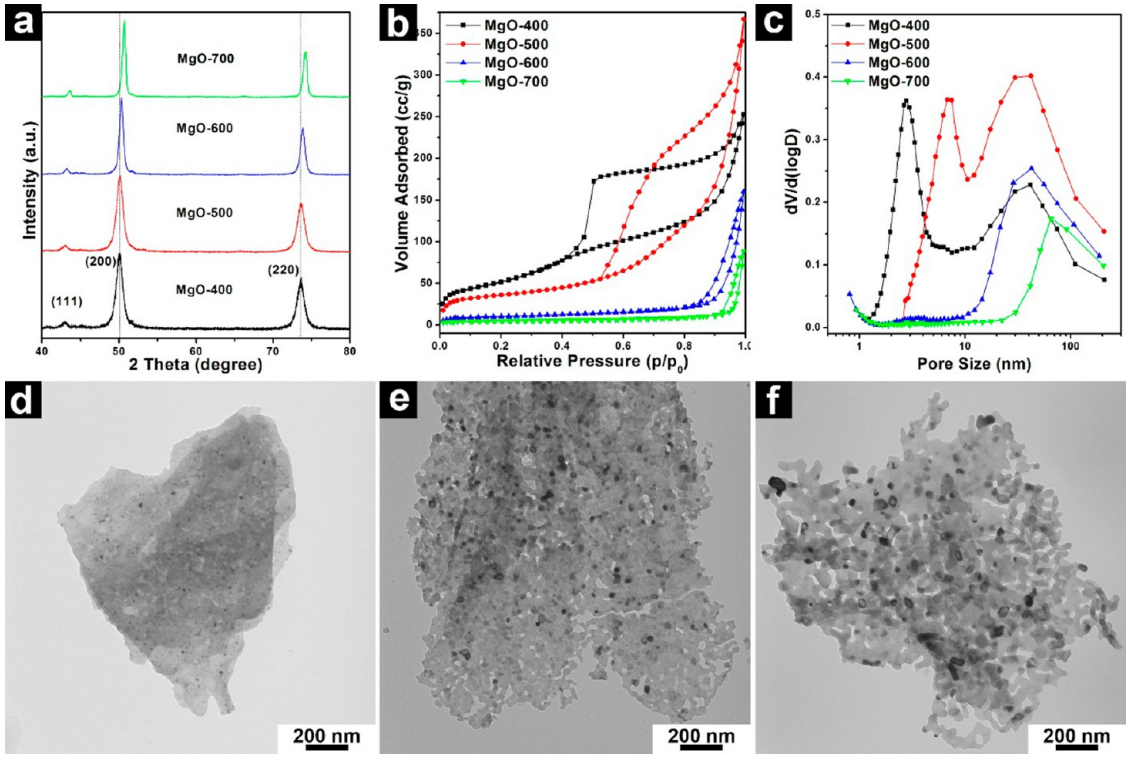

Figure 4. (a) XRD patterns, (b) N_2 adsorption−desorption isotherms, (c) pore size distributions of MgO samples prepared at different calcination temperatures; TEM images of (d) MgO-400, (e) MgO-600, (f) MgO-700.

temperature (such as 500 °C) has no influence on the final hierarchical morphology (Figure 1a). Combining the XRD and SEM results together, it is reasonable to speculate that the microrods observed in SEM are nesquehonite while the hierarchical microspheres are hydromagnesite. Considering the products synthesized at 80 °C show the most uniform hierarchical microspherical morphology, 80 °C is chosen as the aging temperature for time-dependent study.

Effect of Aging Time. To understand the structure and morphology evolution during aging, we varied the aging time from 0.5 to 120 min while the aging temperature was kept at 80 °C. Figure S4 shows the XRD patterns of MgO-P collected at different time intervals. With an aging time less than 5 min, pure nesquehonite phase are obtained (Figure S1a, Figures S4a−c). The hydromagnesite phase begins to appear after aging for 10 min (Figure S4d). With the aging time prolonged to 20 min, the amount of hydromagnesite increases, as evidenced by the increase in intensity of the diffraction peaks (Figure S4e). With an aging time of 30 min or more, pure hydromagnesite phase can be obtained (Figures S4f and S2a).

DOI: 10.1021/acsami.5b05553
ACS Appl. Mater. Interfaces 2015, 7, 21278−21286

Figure 3 shows the SEM images of MgO-P prepared with different aging time. With the aging going on, a morphological evolution from zero-dimensional (0D) nanoparticle to one-dimensional (1D) microrod and then three-dimensional (3D) hierarchical microsphere can be observed. Without aging, the nesquehonite shows a nanoparticulate morphology (Figure S1b). Nesquehonite microrods begin to form in 0.5 min after aging at 80 °C (Figure 3a); the microrods dominate in the product in 2 min (Figure 3b); and almost pure microrods are obtained in 5 min (Figure 3c). With the aging time prolonged to 10 min, hydromagnesite microspheres (indicated by white arrows in Figure 3d) begin to form in the product. With an aging time of 20 min, the 1D rodlike structure disappears and 3D hierarchical microspheres are obtained (Figure 3e). The nesquehonite can be completely converted into hydromagnesite hierarchical microspheres in 30 min (Figure 3f).

It should be noted that the flow rate of precursor solution (10.5 mL min^{-1}) is an important factor for generating distinguished microspherical hierarchical morphology. When low flow rates (1.5 and 6.0 mL min^{-1}) were used, only random flake-like MgO-P precipitates were obtained (Figure S5). As an aging step was employed, Ostwald ripening effect could be applied to explain this observation. When higher feeding flow rate was used, more and smaller nuclei would be created. Then, during aging process, distinguished microspherical hierarchical nanostructures could grow at the expense of nuclei.

Effects of Calcination Temperature. To study the effects of calcination temperature on the structure, arsenic adsorption performance, and antibacterial activity, we varied the calcination temperature from 400 to 700 °C. Figure 4a shows the XRD patterns of the MgO samples prepared at different calcination temperatures. All these patterns can be indexed to face-centered cubic MgO with a periclase phase (JCPDS Card No. 03-0998). Taking MgO-400 as an example, it shows three broad diffraction peaks at around 43.0, 50.0 and 73.5°, which can be indexed to the (111), (200), and (220) reflections of MgO, respectively. The XRD patterns of the other samples generally resemble that of MgO-400. Taking a close look at Figure 4a, two trends can be observed. First, the diffraction peaks sharpen sequentially with the increase of calcination temperature, indicating the increased crystallinity. The average crystallite size determined by Scherrer Equation increases from 8 to 18 nm with the increase of calcination temperature from 400 to 700 °C. Second, the diffraction peaks shift to higher 2θ value gradually with the increase of calcination temperature, indicating a very small extent decrease (0.077%) in lattice.

The porous structure of MgO calcined at different temperatures has been studied by nitrogen sorption analysis. Figure 4b,c shows the adsorption−desorption isotherms and the corresponding pore size distributions of MgO samples, respectively. With the increase of calcination temperature, the capillary condensation shifts to higher relative pressure (Figure 4b). Similar to MgO-500, MgO-400 shows also two sets of nanopores. The relatively smaller mesopores centered at 2.6 nm for MgO-400 is smaller than that for MgO-500 (7.5 nm). For MgO-600 and MgO-700, only large pores associated with the packing voids are observed while the smaller pores cannot be seen.

To understand the origin of small mesopores, TEM images of samples calcined at different temperature were recorded. MgO nanosheets were peeled from the hierarchical spheres by sonication. Compared to MgO-500 (Figure 1c), it is difficult to clearly observe the small mesopores in MgO-400 with a pore size of 2.6 nm (Figure 4d). However, irregular nanopores with large pore size are clearly discerned for both MgO-600 and MgO-700 (Figure 4e,f). Considering the grain size increase in MgO samples with increased calcination temperature (Figure 4a), it is postulated that the relatively small mesopores observed in MgO-400 and MgO-500 come from the nanovoids confined in nanocrystallite of MgO. The size of nanovoids increases with the size of nanocrystallites. Thus, with increasing calcination temperature, both sizes of nanocrystallites and mesopores enlarged. For MgO-600 and MgO-700, the enlarged mesopores are interconnected by the bigger voids formed by nanosheets packing, and cannot be differentiated by a nitrogen sorption analysis. Thus, only one broad pore size distribution peak can be observed in both MgO-600 and MgO-700 samples.

With the increase of calcination temperature from 400 to 700 °C, the surface area of four MgO samples decreases consistently (Table 1). The change of the total pore volume with calcination temperature follows a similar trend, except MgO-500 shows the highest pore volume of 0.57 cm^3g^{-1} among four samples. Compared to MgO-400 with the pore volume of 0.39 cm^3g^{-1}, the increase in pore volume for MgO-500 mainly comes from the capillary condensation at a higher relative pressure range (P/P_0 > 0.90, see Figure 4b,c), which is associated with the packing voids by nanosheets or particles rather than intrinsic pore volume. With the increasing calcination temperature, the crystallinity of MgO framework increases, and thus, the surface area and pore volume decrease.

Table 1. Textural Properties and As(III) Adsorption Capacity for MgO

samples	S_{BET} (m^2 g^{-1})	V_p (cc g^{-1})	pore size (nm)	crystallite size (nm)	As(III) adsorption capacity (mg g^{-1})
MgO-400	194	0.39	2.6	8	545
MgO-500	122	0.57	7.5	10	502
MgO-600	34	0.25	42.5	13	339
MgO-700	16	0.14	64.9	18	148

Arsenic Adsorption Performance. Hierarchical micro/nano-structures with high surface area are very attractive in water treatment due to their high ability to absorb a large amount of pollutants.[6,7] Inspired by this idea, we adopted the MgO hierarchical microspheres for As(III) capture from aqueous solution. The As(III) adsorption capacity is found to be highly dependent on the calcination temperature. With an initial As(III) concentration of 400 ppm, MgO-400 shows the highest adsorption capacity of 545 mg g^{-1}, while MgO-700 shows the lowest adsorption capacity of 148 mg g^{-1} (Figure 5a). Compared with previous literatures where the materials were prepared by a hydrothermal process above 100 °C, the MgO-400 shows adsorption performance superior to that of MgO porous nanoflakes and flower-like MgO but comparable to that of nest-like MgO.[16,17] Furthermore, when compared with other type of As(III) adsorbents from metal oxide group and commercially available arsenic adsorbent, MgO microsphere generally shows higher affinity toward As(III) (Table S1). The highest adsorption performance shown by MgO-400 is attributed to the highest surface area of MgO-400. The high surface area offers more number of adsorption sites and thus improves the adsorption capacity.[24] Additionally, when the crystallite size is correlated to the adsorption capacity of As(III), there exists a linear negative correlation (Figure 5b). This suggested that the crystallite size may also play a role in

DOI: 10.1021/acsami.5b05553
ACS Appl. Mater. Interfaces 2015, 7, 21278−21286

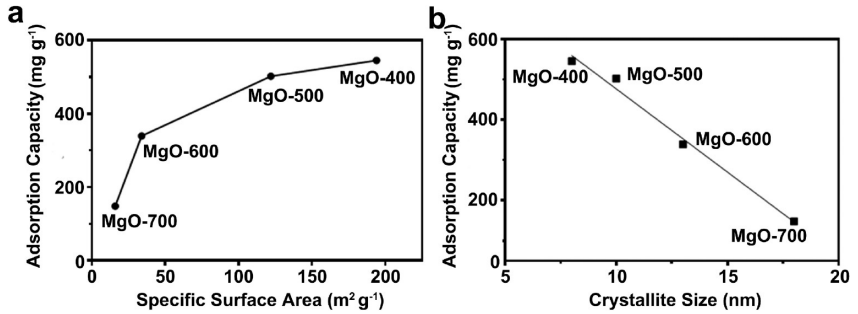

Figure 5. (a) Adsorption capacity as a function of surface area and (b) crystallite size of MgO-400, MgO-500, MgO-600, and MgO-700.

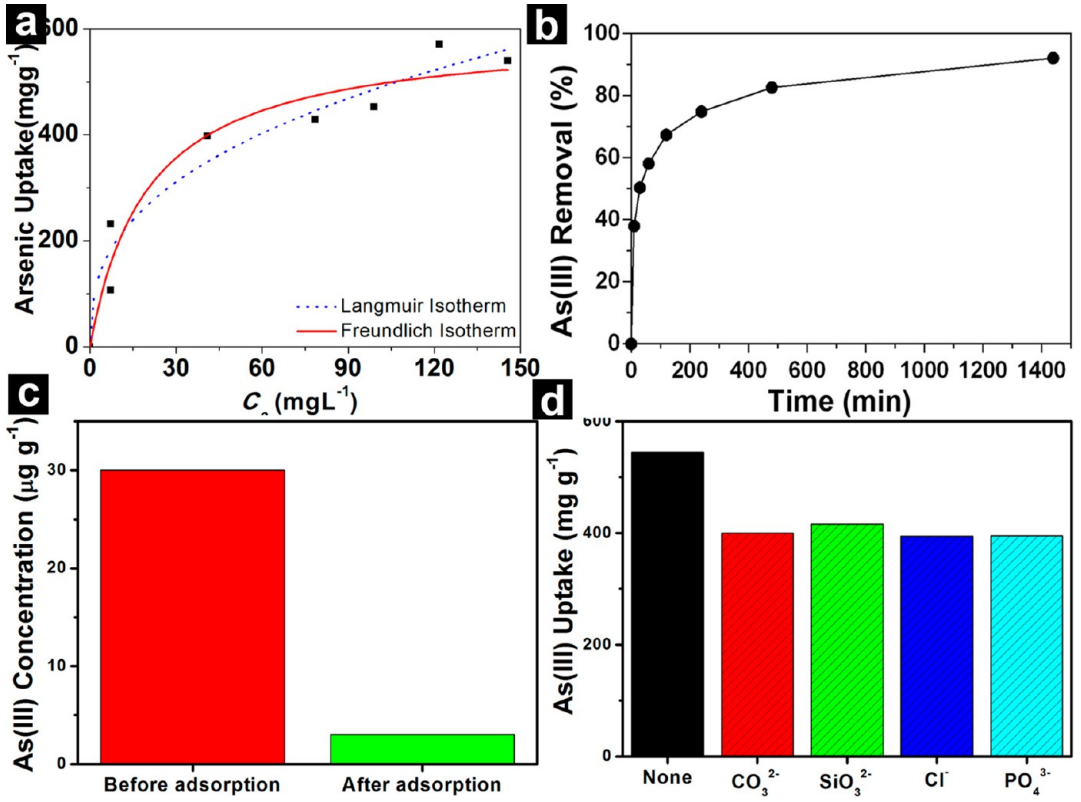

Figure 6. (a) As(III) adsorption isotherm, (b) arsenic removal Percentage during 24 h adsorption with initial As(III) concentration of 200 mg L^{-1}, (c) the adsorption performance at low As concentration, (d) the effect of competing anions on the arsenic adsorption performance of MgO-400 with initial As(III) concentration of 400 mg L^{-1}.

controlling the As(III) adsorption capacity. Similar observation was also reported by Wang and co-workers. They found that the crystallite size of ferrihydrate and magnetite had an effect on the phosphate adsorption.[25] Meanwhile, Yean and co-workers also found that crystallite size of magnetic affected arsenic adsorption reactivity. Their result indicated that smaller crystallite size of magnetite had higher adsorption affinity for As(III) and As(V).[26]

Bearing the As(III) adsorption capacity of different MgO samples in mind, MgO-400, the sample with the highest As(III) uptake, was selected for more detailed As(III) removal study. Figure 6a shows the As(III) adsorption isotherm of MgO-400. With the increased initial concentration (C_0) or equilibrium concentration (C_e), the As(III) uptake amount increased. The results showed that both Langmuir and Freundlich models could simulate the adsorption isotherm curve (R^2 > 0.93). From Langmuir model, the maximum adsorption capacity (q_{max}) and Langmuir constant (K_L) were estimated to be 595 mg g^{-1} and 0.040 L mg^{-1}, respectively, at 25 °C. For MgO-400, from Freundlich model K_F and n value obtained were 87 mg $g^{-1(1-1/n)}$ and 2.6, respectively. This n value, falling between 2 and 10, suggests that the arsenite anions can be easily adsorbed.[9]

As another important aspect for an adsorbent, the adsorption kinetics was also studied (Figure 6b). The adsorption takes place rapidly in the first 120 min and slows down considerably afterward. With an initial As(III) concentration of 200 ppm, 83% of As(III) can be removed in 480 min. The kinetics experimental data fits well with the pseudo-second-order kinetic model with a high correlation coefficient (R^2) of 0.99. A pseudo second-order suggests that the adsorption depends on both the adsorbate and the adsorbent, and it involves chemisorption as well as physiosorption.[27]

The adsorption performance at low As concentration is of significant importance because an As concentration as low as 10 μg L^{-1} may increase the chance of skin cancer.[28] Considering

DOI: 10.1021/acsami.5b05553
ACS Appl. Mater. Interfaces 2015, 7, 21278−21286

this, we studied the adsorption performance of MgO-400 at a low As(III) concentration of 30 μg L^{-1}, which is the estimated arsenic occurrence in groundwater. As shown in Figure 6c, after adsorption for 24 h, the As(III) concentration can be decreased from 30 to 3 μg L^{-1}, indicating that 90% of As(III) has been removed. The As(III) concentration after adsorption is well below the World Health Organization's standard of arsenic limit in drinking water, which is 10 μg L^{-1}.[29]

Wastewater and drinking water normally contain various anions, which may compete with the arsenite ions in the adsorption process. To investigate the effect of competing anions on the arsenic adsorption performance, adsorption in the presence of various foreign anions are performed. As shown in Figure 6d, the As(III) adsorption capacity of MgO-400 is suppressed by 23−27% in the presence of 1 g L^{-1} of phosphate (PO_4^{3-}), carbonate (CO_3^{2-}), silicate (SiO_3^{2-}) and chloride (Cl^-). No significant difference can be observed between different competing anions. Similar "suppression effect" of foreign anions on As adsorption has also been reported by other researchers.[30]

The leaching of magnesium ions into water and arsenic solution was also studied, which reflects the stability of MgO samples. After shaking in Milli-Q water and arsenic solution at 200 rpm for 24 h, the concentration of magnesium is between 0.9−11.8 mg L^{-1} and 3.4−9.9 mg L^{-1}, respectively (Table S2). The leached concentration of Mg^{2+} ions from MgO-400 to the treated solution was around 6.8 mg L^{-1}. Even after 24 h, the amount of MgO leached into the solution is less than 3% from initial amount of absorbent, indicating the stability of this material. In addition to that, this amount is considered to be safe as there is neither maximum contaminant level for magnesium in water nor scientific evidence of magnesium toxicity.[31,17]

To further confirm the stability of MgO adsorbent, we further conducted desorption experiment of spent MgO adsorbent. Referred to desorption study conducted by Payne and Abdel-Fattah,[32] we performed a desorption study of spent MgO adsorbent in the water medium. This experiment was carried out by dispersing the spent adsorbent with a concentration of 0.4 g L^{-1} in water. Then, the suspension was shaken (200 rpm) at room temperature for 24 h with N_2 purging. Spent adsorbent used here was MgO-400 after adsorption in 400 mg L^{-1} As(III). The MgO adsorbent was separated after 24 h shaking. As(III) concentration in the supernatant was then measured using ICP-OES. In the neutral water medium (pH around 7), the result showed that 4.9% of As(III) was released to water from MgO spent adsorbent after 24 h. It is suggested that in the As(III) containing medium, the released amount of As(III) could be even lower due to a smaller concentration gradient.

Antibacterial Performance. The antibacterial property of the MgO hierarchical microspheres was investigated using *E. coli* as a microbial model. Concentration dependent study was first performed to determine the minimum inhibition concentration (MIC) of the MgO samples against *E. coli*. The MIC value is determined to be 700 μg mL^{-1} for MgO-500 (Figure S6). The antibacterial performances of the MgO samples prepared at different calcination temperatures are then compared and the results are presented in Figure 7a. At 700 μg mL^{-1}, MgO-500 gives the highest inhibition effect against *E. coli* among all the MgO samples, followed by MgO-400, MgO-600, and MgO-700. The last three samples did not show total

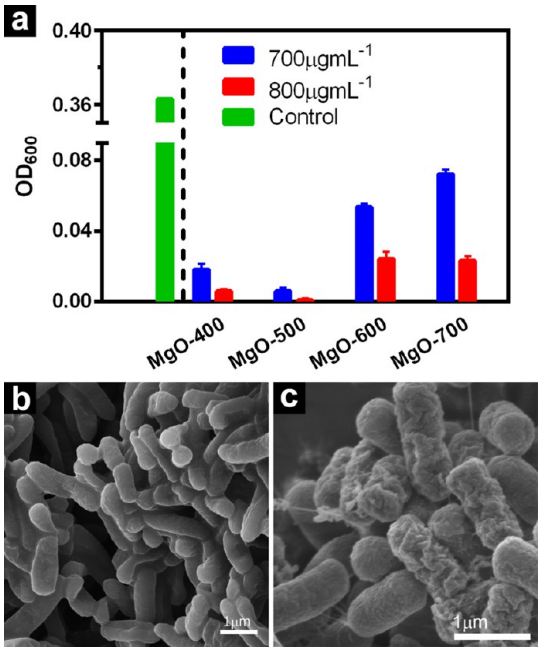

Figure 7. Antibacterial activity of MgO samples prepared at different calcination temperatures (a), SEM images of *E. coli* before (b) and after (c) treatment with MgO-500.

elimination even at 800 μg mL^{-1} showing highest efficacy of MgO microsphere calcined at 500 °C.

The antibacterial efficacy of magnesium oxide is reported to be influenced by both reactive oxygen species (ROS) generation and Mg^{2+} ion release.[20] ROS are proposed to cause membrane damage of bacteria by lipid peroxidation meanwhile the metal ion release in the culture medium is toxic for the bacteria.[20,33] The large specific surface area will enhances the production of reactive oxygen species (ROS) on its surface and thus increase the antibacterial activity.[34] In our study, ROS generated from four MgO samples were measured using DCFH-HA assay with a fluorescence excitation wavelength of 485 nm and emission wavelength of 535 nm.[35] The results are presented in Figure S7. It is shown that after 24 h incubation in LB medium, the amount of ROS generated, indicated by the fluorescence intensity, decrease when the calcination temperature increases, which is in accordance with the surface area of four samples. However, MgO-400 with the highest surface area and highest amount of generated ROS does not show the highest toxicity compared to MgO-500 at the same concentration of 700 μg mL^{-1}, the reason behind this observation should be further studied.

Horie and co-workers revealed that large surface area was not always necessary for cytotoxic activity of metal oxide nanoparticles.[33] To understand the better performance of MgO-500, additional experiments were conducted to measure the release of Mg^{2+} ion in the culture medium and *E. coli* containing culture medium for all MgO samples. The results show that both in culture medium and *E. coli* containing culture medium, MgO-500 released the highest amount of Mg^{2+} ions, 26% more than MgO-400 (Table S2). From the Mg^{2+} release results shown in Table S2, it can be seen that MgO-500 has the highest Mg^{2+} release compared to three other MgO samples in both LB mediums without or with bacteria. It is deduced that the pore structure and crystallinity both affect the Mg^{2+} release. The higher Mg^{2+} release of MgO-500 compared to MgO-400 is

DOI: 10.1021/acsami.5b05553
ACS Appl. Mater. Interfaces 2015, 7, 21278−21286

attributed to its larger mesopore size and higher pore volume (Table 1), which facilitates the solvation and dissolution. However, further increasing the calcination temperature from 500 to 600 and 700 °C causes an increase in crystallinity and a reduction in mesopore volume, leading to slightly decreased Mg^{2+} release. The release of Mg^{2+} ions is also influenced by the medium. Magnesium ion release is reported to be solution-dependent, and the high release of Mg^{2+} both in culture medium and *E. coli*-containing culture medium may be attributed to the type of medium and its content.[36]

The morphology of *E. coli* before and after the treatment with MgO-500 (700 μg mL^{-1} for 24 h) was studied by SEM. As shown in Figure 7b, the untreated *E. coli* shows an intact rod-like morphology. After the treatment with MgO-500, significant changes in morphology and cytoplasmic membrane integrity can be observed (Figure 7c). The treated *E. coli* lose their cellular integrity and shrank from regular rod-likes structure to irregular shape forming pit on their surface. The shrinkage of *E. coli* cytoplasmic membrane is an indication of cell death.[37]

Dual Function of MgO-500. To evaluate the dual functionality of the MgO hierarchical microspheres, water containing both As(III) and *E. coli* was used as the model contaminated water. The sample with the best trade-off between As(III) adsorption and antibacterial performance (MgO-500) was selected for the dual functionality study. With a adsorbent dosage of 0.7 g L^{-1}, the MgO-500 simultaneously adsorbs 90% of the As(III) and kills 100% of *E. coli* in the contaminated water model (Figure 8). In this dual

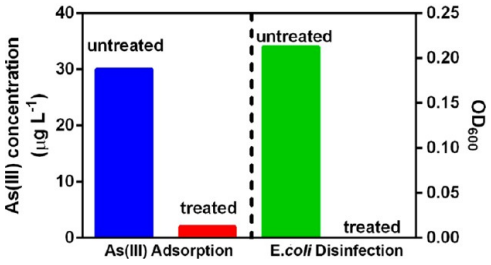

Figure 8. Dual function performance of MgO-500 in a model contaminated water containing both As(III) (30 ppb) and *E. coli*.

function experiment, the amount of Mg^{2+} released was measured as 208 ppm (Table S2). Compared to the contaminated water containing As(III) only, which is at low concentration (Figure 6c), the As(III) adsorption performance is not affected by the presence of *E. coli*. Similarly, the presence of As (III) at 30 ppb in the water model has no toxicity to the *E. coli* when compared to that in the presence of MgO, indicating the role of MgO solely as a disinfection agent. In contrast, after 24 h the model water without addition of MgO shows negative results, that is, arsenic concentration and OD value gave similar measurements with the untreated one. It is therefore demonstrated that the MgO hierarchical microspheres can act as dual functional materials for simultaneous water decontamination and disinfection.

CONCLUSION

In conclusion, a facile and low-cost precipitation−aging−calcination method has been developed for the synthesis of MgO hierarchical microspheres. Our approach offers lower aging temperature and shorter reaction time, compared to other reports, to synthesize hierarchical MgO microspheres, providing low-cost materials beneficial for practical applications. Our study also presents a fundamental understanding on the relationship between synthesis, structure, and dual-functions of MgO materials, which is important for the rational design of multifunctional nanomaterials for simultaneous water decontamination and disinfection applications.

ASSOCIATED CONTENT

Supporting Information

The Supporting Information is available free of charge on the ACS Publications website at DOI: 10.1021/acsami.5b05553.

Additional data on the XRD pattern of hydromagnesite, nequihonite, MgO-P after aging at different temperature and time, The concentration of leached Mg^{2+} into water and arsenic containing solution, in LB medium and LB medium containing bacteria of MgO calcined at 400−700 °C. Minimum inhibitory concentration test of MgO-500 toward *E. coli* and Amount ROS generated by MgO calcined at 400−700 °C in LB medium as indicated by fluorescence intensity. As(III) Comparison of adsorption Capacity of different metal oxide adsorbents and commercial adsorbent. (PDF)

AUTHOR INFORMATION

Corresponding Author

* Email: c.yu@uq.edu.au. Fax: +61 7-33463973.

Author Contributions

The manuscript was written through contributions of all authors. All authors have given approval to the final version of the manuscript.

Notes

The authors declare no competing financial interest.

ACKNOWLEDGMENTS

The authors thank the financial support from the Australian Research Council. The authors acknowledge the Australian National Fabrication Facility and the Australian Microscopy and Microanalysis Research Facility at the Centre for Microscopy and Micro-analysis, The University of Queensland.

REFERENCES

(1) Shannon, M. A.; Bohn, P. W.; Elimelech, M.; Georgiadis, J. G.; Marinas, B. J.; Mayes, A. M. Science and Technology for Water Purification in The Coming Decades. *Nature* **2008**, *452*, 301−310.

(2) Ali, I. New Generation Adsorbents for Water Treatment. *Chem. Rev.* **2012**, *112*, 5073−5091.

(3) Qu, X. L.; Brame, J.; Li, Q. L.; Alvarez, P. J. J. Nanotechnology for a Safe and Sustainable Water Supply: Enabling Integrated Water Treatment and Reuse. *Acc. Chem. Res.* **2013**, *46*, 834−843.

(4) Hua, M.; Zhang, S. J.; Pan, B. C.; Zhang, W. M.; Lv, L.; Zhang, Q. X. Heavy Metal Removal from Water/Wastewater by Nanosized Metal Oxides: A Review. *J. Hazard. Mater.* **2012**, *211*, 317−331.

(5) Yavuz, C. T.; Mayo, J. T.; Yu, W. W.; Prakash, A.; Falkner, J. C.; Yean, S.; Cong, L. L.; Shipley, H. J.; Kan, A.; Tomson, M.; Natelson, D.; Colvin, V. L. Low-field Magnetic Separation of Monodisperse Fe_3O_4 Nanocrystals. *Science* **2006**, *314*, 964−967.

(6) Hu, J. S.; Zhong, L. S.; Song, W. G.; Wan, L. J. Synthesis of Hierarchically Structured Metal Oxides and Their Application in Heavy Metal Ion Removal. *Adv. Mater.* **2008**, *20*, 2977−2982.

(7) Wang, B.; Wu, H. B.; Yu, L.; Xu, R.; Lim, T. T.; Lou, X. W. Template-Free Formation of Uniform Urchin-like α-FeOOH Hollow Spheres with Superior Capability for Water Treatment. *Adv. Mater.* **2012**, *24*, 1111−1116.

DOI: 10.1021/acsami.5b05553
ACS Appl. Mater. Interfaces 2015, 7, 21278−21286

(8) Wu, Z. X.; Li, W.; Webley, P. A.; Zhao, D. Y. General and Controllable Synthesis of Novel Mesoporous Magnetic Iron Oxide@ Carbon Encapsulates for Efficient Arsenic Removal. *Adv. Mater.* **2012**, *24*, 485−491.
(9) Emmanuelawati, I.; Yang, J.; Zhang, J.; Zhang, H. W.; Zhou, L.; Yu, C. Z. Low-Cost and Large-Scale Synthesis of Functional Porous Materials for Phosphate Removal with High Performance. *Nanoscale* **2013**, *5*, 6173−6180.
(10) Yang, J.; Zhou, L.; Zhao, L. Z.; Zhang, H. W.; Yin, J. N.; Wei, G. F.; Qian, K.; Wang, Y. H.; Yu, C. Z. A Designed Nanoporous Material for Phosphate Removal with High Efficiency. *J. Mater. Chem.* **2011**, *21*, 2489−2494.
(11) Yang, J.; Zhang, H. W.; Yu, M. H.; Emmanuelawati, I.; Zou, J.; Yuan, Z. G.; Yu, C. Z. High- Content, Well- Dispersed γ-Fe-2 O-3 Nanoparticles Encapsulated in Macroporous Silica with Superior Arsenic Removal Performance. *Adv. Funct. Mater.* **2014**, *24*, 1354−1363.
(12) Gao, C. L.; Zhang, W. L.; Li, H. B.; Lang, L. M.; Xu, Z. Controllable Fabrication of Mesoporous MgO with Various Morphologies and Their Absorption Performance for Toxic Pollutants in Water. *Cryst. Growth Des.* **2008**, *8*, 3785−3790.
(13) Ai, L. H.; Yue, H. T.; Jiang, J. Sacrificial Template-Directed Synthesis of Mesoporous Manganese Oxide Architectures with Superior Performance for Organic Dye Adsorption. *Nanoscale* **2012**, *4*, 5401−5408.
(14) Zhou, J. B.; Yang, S. L.; Yu, J. G. Facile Fabrication of Mesoporous MgO Microspheres and Their Enhanced Adsorption Performance for Phosphate from Aqueous Solutions. *Colloids Surf., A* **2011**, *379*, 102−108.
(15) Cao, C. Y.; Qu, J.; Wei, F.; Liu, H.; Song, W. G. Superb Adsorption Capacity and Mechanism of Flowerlike Magnesium Oxide Nanostructures for Lead and Cadmium Ions. *ACS Appl. Mater. Interfaces* **2012**, *4*, 4283−4287.
(16) Yu, X. Y.; Luo, T.; Jia, Y.; Zhang, Y. X.; Liu, J. H.; Huang, X. J. Porous Hierarchically Micro-/Nanostructured MgO: Morphology Control and Their Excellent Performance in As(III) and As(V) Removal. *J. Phys. Chem. C* **2011**, *115*, 22242−22250.
(17) Liu, Y.; Li, Q.; Gao, S. A.; Shang, J. K. Exceptional As(III) Sorption Capacity by Highly Porous Magnesium Oxide Nanoflakes Made from Hydrothermal Synthesis. *J. Am. Ceram. Soc.* **2011**, *94*, 217−223.
(18) Jia, Y.; Luo, T.; Yu, X. Y.; Sun, B.; Liu, J. H.; Huang, X. J. A Facile Template Free Solution Approach for The Synthesis of Dypingite Nanowires and Subsequent Decomposition to Nanoporous MgO Nanowires with Excellent Arsenate Adsorption Properties. *RSC Adv.* **2013**, *3*, 5430−5437.
(19) Stoimenov, P. K.; Klinger, R. L.; Marchin, G. L.; Klabunde, K. J. Metal Oxide Nanoparticles as Bactericidal Agents. *Langmuir* **2002**, *18*, 6679−6686.
(20) Leung, Y. H.; Ng, A. M. C.; Xu, X. Y.; Shen, Z. Y.; Gethings, L. A.; Wong, M. T.; Chan, C. M. N.; Guo, M. Y.; Ng, Y. H.; Djurisic, A. B.; Lee, P. K. H.; Chan, W. K.; Yu, L. H.; Phillips, D. L.; Ma, A. P. Y.; Leung, F. C. C. Mechanisms of Antibacterial Activity of MgO: Non-ROS Mediated Toxicity of MgO Nanoparticles Towards *Escherichia coli*. *Small* **2014**, *10*, 1171−1183.
(21) Makhluf, S.; Dror, R.; Nitzan, Y.; Abramovich, Y.; Jelinek, R.; Gedanken, A. Microwave-Assisted Synthesis of Nanocrystalline MgO and Its Use as A Bacteriocide. *Adv. Funct. Mater.* **2005**, *15*, 1708−1715.
(22) Qu, Y.; Zhou, W.; Ren, Z. Y.; Pan, K.; Tian, C. G.; Liu, Y.; Feng, S. S.; Dong, Y. Z.; Fu, H. G. Fabrication of a 3D Hierarchical Flower-Like MgO Microsphere and Its Application as Heterogeneous Catalyst. *Eur. J. Inorg. Chem.* **2012**, *12*, 954−960.
(23) Bian, S. W.; Baltrusaitis, J.; Galhotra, P.; Grassian, V. H. A Template-Free, Thermal Decomposition Method to Synthesize Mesoporous MgO with A Nanocrystalline Framework and Its Application In Carbon Dioxide Adsorption. *J. Mater. Chem.* **2010**, *20*, 8705−8710.
(24) Mandal, S.; Sahu, M. K.; Patel, R. K. Adsorption Studies of Arsenic(III) Removal from Water by Zirconium Polyacrylamide Hybrid Material (ZrPACM-43). *Water Res. Ind.* **2013**, *4*, 51−67.
(25) Wang, X.; Li, W.; Harrington, R.; Liu, F.; Parise, J. B.; Feng, X.; Sparks, D. L. Effect of Ferrihydrite Crystallite Size on Phosphate Adsorption Reactivity. *Environ. Sci. Technol.* **2013**, *47*, 10322−10331.
(26) Yean, S.; Cong, L.; Yavuz, C. T.; Mayo, J. T.; Yu, W. W.; Kan, A. T.; Colvin, V. L.; Tomson, M. B. Effect of Magnetite Particle Size on Adsorption and Desorption of Arsenite and Arsenate. *J. Mater. Res.* **2005**, *20*, 3255−3264.
(27) Abramian, L.; El-Rassy, H. Adsorption Kinetics and Thermodynamics of Azo-Dye Orange II onto Highly Porous Titania Aerogel. *Chem. Eng. J.* **2009**, *150*, 403−410.
(28) Chandra, V.; Park, J.; Chun, Y.; Lee, J. W.; Hwang, I. C.; Kim, K. S. Water-Dispersible Magnetite-Reduced Graphene Oxide Composites for Arsenic Removal. *ACS Nano* **2010**, *4*, 3979−3986.
(29) World Health Organization, *Guidelines for Drinking-Water Quality*. 4th ed.; WHO Press: Switzerland, 2011.
(30) Guan, X. H.; Dong, H. R.; Ma, J.; Jiang, L. Removal of Arsenic from Water: Effects of Competing Anions on As(III) Removal in KMnO4-Fe(II) Process. *Water Res.* **2009**, *43*, 3891−3899.
(31) Salvato, J. A. *Environmental Engineering and Sanitation*; 4th ed. John Wiley & Sons: Hoboken, NJ, 1992.
(32) Payne, K. B.; Abdel-Fattah, T. M. Adsorption of Arsenate and Arsenite by Iron-Treated Activated Carbon and Zeolites: Effects of pH, Temperature, and Ionic Strength. *J. Environ. Sci. Health, Part A: Toxic/Hazard. Subst. Environ. Eng.* **2005**, *40*, 723−49.
(33) Horie, M.; Fujita, K.; Kato, H.; Endoh, S.; Nishio, K.; Komaba, L. K.; Nakamura, A.; Miyauchi, A.; Kinugasa, S.; Hagihara, Y.; Niki, E.; Yoshida, Y.; Iwahashi, H. Association of The Physical and Chemical Properties and The Cytotoxicity of Metal Oxide Nanoparticles: Metal Ion Release, Adsorption Ability and Specific Surface Area. *Metallomics* **2012**, *4*, 350−360.
(34) Sawai, J.; Kojima, H.; Igarashi, H.; Hashimoto, A.; Shoji, S.; Sawaki, T.; Hakoda, A.; Kawada, E.; Kokugan, T.; Shimizu, M. Antibacterial Characteristics of Magnesium Oxide Powder. *World J. Microbiol. Biotechnol.* **2000**, *16*, 187−194.
(35) Applerot, G.; Lellouche, J.; Lipovsky, A.; Nitzan, Y.; Lubart, R.; Gedanken, A.; Banin, E. Understanding The Antibacterial Mechanism of Cuo Nanoparticles: Revealing The Route of Induced Oxidative Stress. *Small* **2012**, *8*, 3326−3337.
(36) Feyerabend, F.; Drucker, H.; Laipple, D.; Vogt, C.; Stekker, M.; Hort, N.; Willumeit, R. Ion Release from Magnesium Materials in Physiological Solutions Under Different Oxygen Tensions. *J. Mater. Sci.: Mater. Med.* **2012**, *23*, 9−24.
(37) Jin, T.; He, Y. P. Antibacterial Activities of Magnesium Oxide (MgO) Nanoparticles Against Foodborne Pathogens. *J. Nanopart. Res.* **2011**, *13*, 6877−6885.

DOI: 10.1021/acsami.5b05553
ACS Appl. Mater. Interfaces 2015, 7, 21278−21286